Coherent description of transport across the water interface: From nanodroplets to climate models

Øivind Wilhelmsen,[1,*] Thuat T. Trinh,[1] Anders Lervik,[1] Vijay Kumar Badam,[2] Signe Kjelstrup,[1] and Dick Bedeaux[1]

[1]*Department of Chemistry, Norwegian University of Science and Technology, Trondheim, Norway*

[2]*Institute of Fluid Mechanics (LSTM), Friedrich-Alexander-Universität Erlangen-Nürnberg, Cauerstrasse 4, D-91058 Erlangen, Germany*

(Received 28 August 2015; revised manuscript received 15 December 2015; published 14 March 2016)

Transport of mass and energy across the vapor-liquid interface of water is of central importance in a variety of contexts such as climate models, weather forecasts, and power plants. We provide a complete description of the transport properties of the vapor-liquid interface of water with the framework of nonequilibrium thermodynamics. Transport across the planar interface is then described by 3 interface transfer coefficients where 9 more coefficients extend the description to curved interfaces. We obtain all coefficients in the range 260–560 K by taking advantage of water evaporation experiments at low temperatures, nonequilibrium molecular dynamics with the TIP4P/2005 rigid-water-molecule model at high temperatures, and square gradient theory to represent the whole range. Square gradient theory is used to link the region where experiments are possible (low vapor pressures) to the region where nonequilibrium molecular dynamics can be done (high vapor pressures). This enables a description of transport across the planar water interface, interfaces of bubbles, and droplets, as well as interfaces of water structures with complex geometries. The results are likely to improve the description of evaporation and condensation of water at widely different scales; they open a route to improve the understanding of nanodroplets on a small scale and the precision of climate models on a large scale.

DOI: 10.1103/PhysRevE.93.032801

I. INTRODUCTION

Water is arguably the most important substance to mankind, and its peculiarities keep attracting attention in the literature. The water nucleation in clouds studied in atmospheric sciences [1,2], the intriguing behavior of cavitation of water at large negative pressures [3–7], and the mysterious second liquid phase in supercooled water [8,9] are some examples where the phase transitions of water are central. The properties of water have puzzled researchers for centuries. Since the polar water molecules form strong intermolecular hydrogen bonds, water behaves very differently from nonpolar substances such as hydrocarbons, and even polar substances such as sulfur dioxide.

Evaporation and condensation of water are of importance not only in industry, but also in the modeling of natural phenomena. Stevens and Bony highlighted water precipitation and circulation as some of the largest sources of uncertainty in global climate models [10]. In nature, the formation, intensity, and propagation of hurricanes depend on evaporation at sea level and condensation into clouds [11]. In industry, most of the world's electricity is generated by running steam turbines, where steam is condensed back to liquid water at every cycle. Further progress on these areas and many others relies on a precise description of transport of heat and mass across the vapor-liquid interface of water. We shall provide such a description in this work.

In engineering applications, the typical treatment of interfaces assumes that the resistance of diffusive films near the interface dominates, neglecting thereby the resistance of the interface itself [12–14]. This assumption contradicts experiments and simulations that document a "temperature jump" across the interface [15–22]. Temperature jumps during steady-state evaporation of water as large as 7.8 K were reported for the first time by Ward, Fang, and Stanga [15–17]. Since then, experiments of higher accuracy have been carried out by using a PVC container to reduce the heat leak, giving temperature jumps of an astounding 15.69 K [21,22].

Van der Ham *et al.* showed that the interface resistance should be included for accurate description of phase transitions in distillation columns [23]. Furthermore, the interface resistances dominate at the nanoscale, e.g., in nucleation processes or for transport of heat and mass through nanointerfaces [24,25]. For nanoscopic bubbles and droplets, the influence of curvature is large and should be taken into account [25,26].

Several theories provide a description of evaporation and condensation, taking into account the resistance of the interface. These include kinetic gas theory, see, e.g., Ref. [27], statistical rate theory [15–17,20], and nonequilibrium thermodynamics [14]. Kinetic gas theory (KGT) describes the behavior of the interface in terms of velocity distribution functions, and has resulted in the well-known Hertz-Knudsen equation and its extensions which predict the net mass flux during evaporation and condensation [28]. These formulas include the evaporation (or condensation) coefficient as an empirical parameter. When calculated from experiments with nominally the same experimental conditions, the evaporation coefficients differ widely from each other [29]. Bond and Struchtrup argued that, contrary to classical KGT, the condensation coefficient should depend on the impact energy of the condensing particle, and that the evaporation and condensation mass flux is mostly driven by energy flow to the interface [28,29]. Another major challenge in KGT is to properly incorporate the internal degrees of freedom of the water molecules. For these reasons, KGT is today unable to predict the condensation/evaporation rate of water to a sufficient accuracy [21,28].

Statistical rate theory (SRT) was developed to predict the net mass flux during evaporation [15–17,20–22]. The evaporation rate is here expressed in terms of an evaporation

*oivind.wilhelmsen@sintef.no

probability, defined through the entropy change of a molecule going from the liquid phase to the vapor phase. The expression for the mean square velocity of a particle is used for the unidirectional flux. SRT has in its original formulation the advantage of no fitting parameters [15]. It has been used successfully to predict the evaporation rates of n-octane and water [16,22]. Recent discussions have pointed out that SRT does not provide an expression for the interfacial energy flux, which plays a leading role in determining the interface temperature jump as discussed in the literature [21,28].

We shall in this work describe evaporation and condensation with nonequilibrium thermodynamics (NET). NET has been envisioned by several authors as the most promising candidate to provide a general yet precise description of transport across interfaces [21,28,30]. The formalism carefully states how transfer across the interface depends on the conditions in the nearby phases, and consistently takes into account coupling effects, using a set of interface transfer coefficients. A major shortcoming of NET is that these coefficients are unavailable for most substances [21,28,30]. However, NET as a general theory has been crucial to understand a large variety of phenomena, ranging from polymer melts [31] and thermoelectric generators [32] to polarization of water molecules in thermal gradients [33]. While KGT and SRT are useful tools for specific cases, NET is a more general and far-reaching theory.

In this work, we obtain the interface transfer coefficients along the vapor-liquid coexistence line of water, from supercooled water at 260 K to near the critical point at 560 K. To the best of our knowledge, our work is the first to accomplish this for the complicated case of water. Results for the Lennard-Jones system were reported previously, for flat as well as curved interfaces [34]. Our long-range aim is to provide systematic information on interface transfer coefficients. In this work, we use an approach taking advantage of water-evaporation experiments at low temperatures [21], boundary-driven nonequilibrium molecular dynamics with the TIP4P/2005 rigid-water-molecule model at high temperatures [34], and a mesoscopic description with square gradient theory to complement the picture [26]. Square gradient theory can be extrapolated to ranges where experiments are unavailable or simulations are unfeasible. This enables, for the first time, a consistent description of transport of heat and mass across planar and curved vapor-liquid interfaces of water with nonequilibrium thermodynamics. We shall discuss how these results can be used to improve current climate models.

II. THE METHODOLOGY

The vapor-liquid coexistence line of water ranges from the triple point at 273 K and 612 Pa to the critical point at 647 K and 22 MPa, as illustrated in Fig. 1. Moreover, water can be supercooled down to an astounding 231 K at atmospheric pressure [36]. In fact, most of the experiments relevant for this work involve supercooled water. To calculate the interface transfer coefficients from NET requires information about heat and mass fluxes as well as temperatures and pressures (or densities) in the bulk phases adjacent to the interface. To the best of our knowledge, only the experiments by Badam *et al.* [21], represented by the shaded area in Fig. 1, are sufficiently equipped to be useful in this context. The interface transfer coefficients can also be obtained using nonequilibrium molecular dynamics (NEMD), where water-like particles described, for instance, with the TIP4P/2005 model are simulated [37]. Due to the large difference between the vapor and liquid phase densities for water, and the complicated interaction potential, NEMD simulations with TIP4P/2005 are only feasible down to a temperature in the liquid phase of $T \sim 480$ K. The vapor phase requires a minimum number of particles for the thermostats to be functional and the fluctuations to be acceptable. Due to the low vapor-phase density, the total number of particles and simulation volume necessary to achieve this at low temperatures are enormous and lead to computational demands exceeding what is currently available. For instance, simulations at $T = 350$ K would require several million particles and a μm simulation volume, resulting in a simulation time of years, even for the most powerful supercomputers available today.

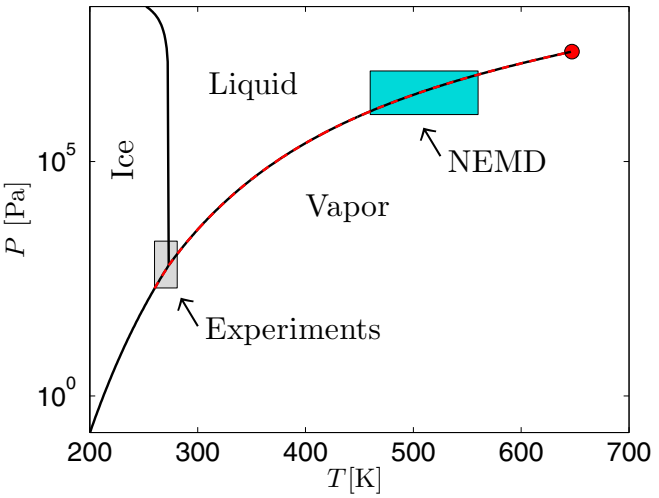

FIG. 1. The phase-diagram of water [35], with the range of available experimental data and the range where NEMD and SGT (red-dashed line) are feasible. The red circle is the critical point.

At sufficiently high temperatures, e.g., in the vicinity of the critical point, the interface ceases to be a barrier to transport. The most interesting domain to obtain interface transfer coefficients from NEMD simulations is therefore between ~480–550 K as shown in the figure.

Another powerful tool, not restricted by computational time or the large density difference between the phases, is square gradient theory (SGT). We shall use the available experiments (left shaded region in Fig. 1) and NEMD simulations (right shaded region in Fig. 1) to calibrate the description with SGT [24,34]. This allows us to obtain the interface transfer coefficients along the entire coexistence line, also where experiments are unavailable or NEMD simulations are impossible. A major benefit of this approach is that SGT can be used to find the curvature dependence of the interface transfer coefficients.

We give first an introduction to nonequilibrium thermodynamics for interfaces (Sec. II A), before we describe the experiments (Sec. II B), the NEMD simulations (Sec. II C), and the SGT formulation (Sec. II D).

A. Nonequilibrium thermodynamics

Transport of heat and mass across interfaces can be described consistently with NET. In a single-component system, the formulation is [14]

$$\frac{1}{T^{\mathrm{o}}} - \frac{1}{T^{\mathrm{i}}} = R_{qq} J_q'^{\mathrm{o}} + R^{\mathrm{o}}_{q\mu} J, \tag{1}$$

$$-\left(\frac{\mu^{\mathrm{o}}}{T^{\mathrm{o}}} - \frac{\mu^{\mathrm{i}}}{T^{\mathrm{i}}}\right) + h^{\mathrm{o}}\left(\frac{1}{T^{\mathrm{o}}} - \frac{1}{T^{\mathrm{i}}}\right) = R^{\mathrm{o}}_{\mu q} J_q'^{\mathrm{o}} + R^{\mathrm{o}}_{\mu\mu} J, \tag{2}$$

where the superscripts i and o indicate the values just inside or outside the interface, respectively. Furthermore, J_q' is the measurable heat flux, J is the mass flux, μ is the chemical potential, h is the specific enthalpy, and R_{ij} are the *overall* interface transfer coefficients, known as interface resistivities [14,38]. Following Onsager, the matrix of coefficients is symmetric, $R_{q\mu} = R_{\mu q}$. This equality, which has been verified by simulations [38], means that there are only 3 independent resistivities for heat and mass transfer across the interface. These coefficients can be expanded in the total curvature, $H = \kappa_1 + \kappa_2$, and the Gaussian curvature, $K = \kappa_1\kappa_2$ [25]:

$$R_{ij} = R_{ij,0}\left[1 + d_{ij}H + \nu_{ij}(d_{ij}H)^2 + \bar{\nu}_{ij} d_{ij}^2 K\right], \tag{3}$$

where κ_1 and κ_2 are the principal curvatures and subscript 0 refers to the planar interface. The length, d_{ij}, gives the typical size of a droplet where curvature corrections become important, while ν_{ij} and $\bar{\nu}_{ij}$ are scalars which decide the importance of the second-order corrections. The coupling of heat and mass can also be formulated using the quantity called the *heat of transfer*, defined as

$$q^{*\mathrm{o}} = \left(\frac{J_q'^{\mathrm{o}}}{J}\right)_{\Delta T=0, J=0} = -\frac{R^{\mathrm{o}}_{q\mu}}{R_{qq}}. \tag{4}$$

The advantage of using the heat of transfer is that it has the same units as the enthalpy, and can then easily be compared to, for instance, the vaporization enthalpy.

For a single-component system, the coefficients from NET depend only on the interface temperature, T^s. The concept of interface temperature assumes that the interface can be described as a separate thermodynamic system which is autonomous, i.e., in local equilibrium. Local equilibrium in this context means that interfacial properties, such as the surface tension, the interface transfer coefficients, and other thermodynamic excess variables in a system which is globally at *nonequilibrium*, have the same values as in a system at *equilibrium* at the temperature T^s. The assumption of local equilibrium of the interface has been verified several times, with both theory and simulations [39,40]. Local equilibrium of the interface gives rise to many exciting properties, discussed for instance by Savin *et al.* [41]. One of them was stated by Johannessen and Bedeaux [39]:

$$\rho^l - \rho^g = \rho^l_{\mathrm{sat}}(T^s) - \rho^g_{\mathrm{sat}}(T^s), \tag{5}$$

where ρ^l and ρ^g are the values of the bulk densities of liquid and vapor respectively, extrapolated to the dividing surface, and subscript "sat" refers to the properties along the vapor-liquid coexistence line. Since the difference in density between the liquid and vapor of water is enormous, in particular at low temperatures, Eq. (5) tells us that $\rho^l = \rho^l_{\mathrm{sat}}(T^s)$. Experiments show that the pressure during steady-state evaporation is very close to the saturation pressure at T^l [21]. Consequently, $T^s \simeq T^l$. This relation is certainly true for the experiments in the left part of Fig. 1, since the vapor pressure is only a few hundred pascals. We shall verify numerically that it is also true for the NEMD simulations.

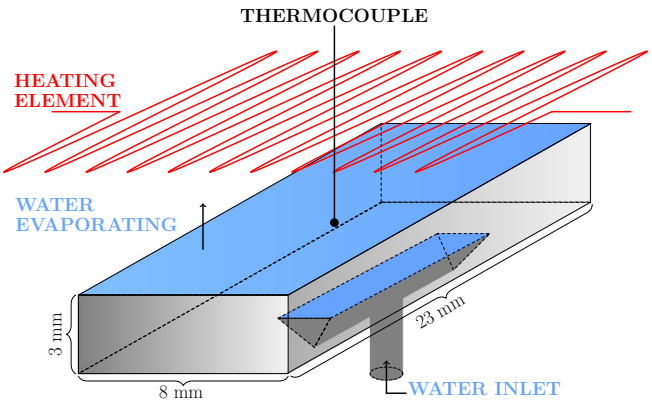

FIG. 2. The experimental facility where water enters at the bottom and evaporates. A heating element was placed approximately 3 mm above the interface. More details about the facility and the experimental procedure can be found in Ref. [21].

B. The experiments

Badam *et al.* [21] presented in 2007 experiments of water evaporation, using the well-equipped experimental facility depicted in Fig. 2. The rectangular evaporation channel was made by PVC to avoid thermocapillary convection and make the heat transfer along the channel walls as small as possible. A water inlet was placed at the center location at the bottom of the channel, and distilled deionized water was used in the experiments. Before the experiments, the chamber was evacuated for about 12 hours to a pressure of about 1–10 Pa, and water was introduced without exposure to air.

A steady-state evaporation rate was obtained by adjusting the flow rate of water, and the system was considered to be in steady state when the interface remained at a stable position (within ± 10 μm) for about 2–3 hours. At steady state, a movable 25 μm thermocouple was used to obtain temperature measurements at different positions perpendicular to the interface, both in the vapor phase and in the liquid phase along the center line of the experimental facility, exemplified by the position of the thermocouple in Fig. 2. A heating-element grid was mounted, and during the experiments it was located approximately 3 mm above the water interface. Experiments were carried out with the heating element at different temperatures. The pressure was monitored using a pressure transducer with a mercury manometer as a reference and could be obtained to an accuracy of ± 13 Pa. We refer the reader to Ref. [21] for more details about the experimental facility and procedure.

Using the raw data from these experiments, we have reanalyzed the experimental data using state-of-the-art thermophysical models according to the International Association for the Properties of Water and Steam (IAPWS) formulation [35,42] and in the framework of nonequilibrium thermodynamics,

which means that all temperature measurements and estimated fluxes have been extrapolated to the position of the dividing interface. Let z be the direction perpendicular to the interface, and $z = r_e$ be the position of the interface. The measurable heat flux J'_q at both the vapor and liquid side of the interface can be calculated with the temperature measurements and

$$J'_q|_{z=r_e} = -\lambda(T(r_e),\rho(r_e))\frac{dT(r_e)}{dz}, \tag{6}$$

where λ is the thermal conductivity which depends on the temperature and the density, ρ. At steady state, conservation of mass across the interface implies a constant mass flux, J. The momentum and energy balance equations at the interface ($z = r_e$) are

$$\rho^g(v^g)^2 + p^g = \rho^l(v^l)^2 + p^l + \sigma_0\kappa(T^l), \tag{7}$$

$$h^g + 0.5(v^g)^2 + \frac{J'^g_q}{J} = h^l + 0.5(v^l)^2 + \frac{J'^l_q}{J}, \tag{8}$$

where v is the velocity perpendicular to the interface, $J = \rho v$, σ_0 is the surface tension of the flat interface, and κ is the curvature. From the experiments, p_g,κ,$T(z)$, and $dT(z)/dz$ are known or can be estimated. Simultaneously solving Eqs. (6)–(8) results in the liquid-phase density ρ_l and the mass flux J, from which the left-hand sides of Eqs. (1) and (2) can be calculated. However, there are only two independent equations, but three interface transfer coefficients. We shall use SGT to provide the missing information.

C. Nonequilibrium molecular dynamics

The resistances of the vapor-liquid interface of water to heat and mass transfer below room temperature are enormous, and give temperature jumps which can be measured experimentally. However, these resistances decay exponentially with increasing interface temperature [34], and conventional thermocouples have too high uncertainty to measure the temperature jump at sufficiently high interface temperatures.

In this work, we used NEMD with the TIP4P/2005 model to study the interface of water at higher temperatures [37]. The TIP4P/2005 model has properties which are reasonably similar to water and reproduces many of its anomalous properties [43]. Simulations were performed in LAMMPS [44] using the Velocity-Verlet integrator with an integration time step of 2.0 fs. Lennard-Jones interactions were truncated at a distance of 13 Å, while the long-range Coulombic interactions were handled using the particle-particle-particle-mesh solver [45]. All bonds and angles were constrained using the SHAKE algorithm [46,47] as implemented in LAMMPS. The setup used was similar to the one used by Orsi [48], and we refer to Ref. [48] for further details. Furthermore, we used the well-established procedure from boundary-driven NEMD simulations depicted in Fig. 3. The simulations were carried out in a rectangular simulation volume with the dimensions $\{L_x,L_y,L_z\} = \{62,62,248\}$ Å and a total of 12 500 water molecules. The simulation volume was located at $-0.5L_z \leqslant z \leqslant 0.5L_z$, with a liquid slab located in the middle with vapor phases on each side [49,50]. The temperature gradient was imposed in the z direction by thermostating the region $|z/L_z| < 0.05$ to a low temperature, T_{cold}, and the regions $0.45 < |z/L_z| < 0.5$ to a high temperature, T_{hot}. We used the

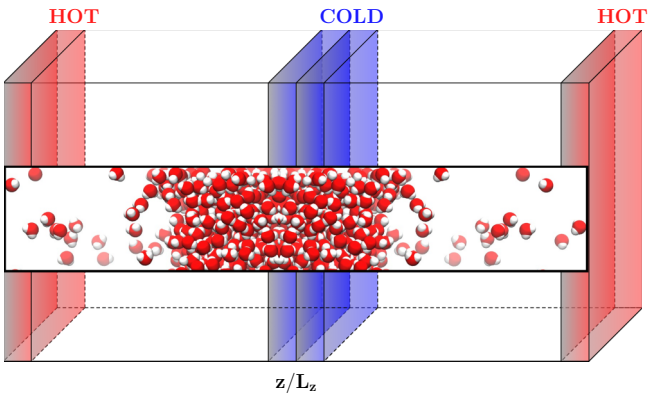

FIG. 3. The setup for the NEMD simulations, where a liquid-phase region thermostated to a low temperature is located at the center, with two vapor phases at each side, thermostated to high temperatures.

Langevin thermostat [51], and T_{hot} was set to $T_{\text{cold}} + 200$ K. Periodic boundary conditions were used and the mass flux was hence zero. At steady state and with zero mass flux, the energy balance gives that the measurable heat flux is constant.

The heat flux can be calculated by using the average kinetic energy, $\overline{\Delta K}$, added (+) or subtracted (−) in the thermostats during the simulation [52]:

$$J_e = J'_q = \pm\frac{\overline{\Delta K}}{2\Delta_t L_x L_y}, \tag{9}$$

where J_e is the total energy flux and Δ_t is the time step between addition or subtraction of kinetic energy in the thermostats. For NEMD simulations with bulk fluids, this approach has proven to give accurate estimates of, for instance, the thermal conductivity [43,52]. However, due to the widely different densities in the two phases, we experienced that the fluctuations in $\overline{\Delta K}$ were so large that the conventional procedure would lead to more than 50% error in the estimated heat flux. A simple test for this was to compare the heat flux from interface-NEMD simulations with NEMD simulations of bulk phases with similar density and temperature gradients. We circumvented this problem by employing the following method:

(1) After the interface-NEMD simulations had reached steady state, the time average density and temperature profiles from the bulk vapor phase were extracted sufficiently far away from the interface region and the thermostats.

(2) Following the routine discussed by Bresme and Armstrong [52], bulk-NEMD simulations were performed using very similar density and temperature profiles to those in the bulk-vapor phase of the interface-NEMD simulations, but with a larger number of particles to have less fluctuations. These simulations gave a mean thermal conductivity of the vapor phase, λ_m.

(3) The heat flux in the interface-NEMD simulations was then calculated using $J'_q = -\lambda_m\overline{dT/dz}$, where $\overline{dT/dz}$ was the mean temperature gradient of the bulk-vapor phase from the interface-NEMD simulations. The temperature profiles were in all cases linear.

The temperature profiles were extrapolated from the liquid and vapor bulk phases to the location of the equimolar dividing surface to obtain T^l and T^g, respectively. Since the mass flux

was zero, the interface transfer coefficient for heat transfer, $R_{qq,0}$, could then be calculated from

$$\left(\frac{1}{T^l}-\frac{1}{T^g}\right)J_q'^{-1}=R_{qq,0}. \tag{10}$$

We developed a SGT formulation which matched the properties of TIP4P/2005 and the magnitude and location of the temperature jump from NEMD. Square gradient theory could then be used to calculate the remaining coefficients $R_{q\mu}$ and $R_{\mu\mu}$ as discussed in Refs. [25,34].

D. Square gradient theory

From the discussions in Secs. II A–II C, it is clear that neither experiments nor NEMD are able to provide the interface transfer coefficients at both high and low temperatures. In addition, nonequilibrium thermodynamics defines two equations [Eqs. (1) and (2)], but there are three unknown coefficients.

Square gradient theory (SGT) is the missing piece to give the complete picture; however, a quantitative description is only possible with input from both experiments (low temperatures) and NEMD (high temperatures). We shall explain in detail how this synergy works, and refer to previous work for details on the SGT formulation [24,26,53,54]. Square gradient theory relies on an equation of state which is capable of capturing the thermodynamic behavior of both the liquid and the vapor.

We shall use the well-known and successful cubic plus association (CPA) equation of state to describe the thermodynamic properties of water [55–57]. In this description, the cubic part (subscript C) accounts for the physical forces and the association part (subscript A) accounts for hydrogen bonding and other chemical forces [56]. This gives for the Helmholtz energy density

$$f_{\rm eos}=f_{\rm eos,C}+f_{\rm eos,A}, \tag{11}$$

from which other relevant properties such as pressure, entropies, and enthalpies can be derived [56]. In this work, the SRK equation was used for $f_{\rm eos,C}$, and the association term, $f_{\rm eos,A}$, was taken from statistical associating fluid theory. The last term sums over all association sites of the water molecules. We used the same CPA formulation as Queimada *et al.* [57], and refer to that work for further details. For real water, we used the parameters found by Queimada *et al.* [57]. However, since TIP4P/2005 gives slightly different properties than real water, we refitted the CPA equation of state for TIP4P/2005, giving parameters reported in Table I in the Appendix. The TIP4P/2005-CPA equation of state reproduces the properties of TIP4P/2005 to a very good accuracy, as shown in Fig. 13 in the Appendix.

Square gradient theory is the first approximation to mass-based density functional theory. A contribution is added to the Helmholtz energy functional proportional to the square of the density gradient [58]:

$$\begin{aligned}F[\rho(\mathbf{r}),T]&=\int d\mathbf{r}[f(\rho(\mathbf{r}),T)]\\&=\int d\mathbf{r}\left[f_{\rm eos}(\rho(\mathbf{r}),T)+\frac{1}{2}\eta(T)|\nabla\rho(\mathbf{r})|^2\right].\end{aligned} \tag{12}$$

Here, $\mathbf{r}$ is the position, $f_{\rm eos}$ is the equation of state value of the Helmholtz energy density in the homogeneous phases, and η is the influence parameter. In this work, we have incorporated a temperature-dependent influence parameter, since the slope of the surface tension of water deviates from other substances, reflecting its anomalous behavior [59]. The function $\eta(T)$ for water was given in Ref. [57]. We have used the same function for TIP4P/2005, but a different set of parameters given in Table I in the Appendix, reproducing the surface tension of TIP4P/2005 within the computational error, as shown in Fig. 14 in the Appendix.

Equilibrium density profiles through the interface region can be obtained by minimizing the Helmholtz energy, keeping the total number of particles constant. This gives a consistent set of thermodynamic variables which depend not only on the temperature and density, but also on spatial derivatives of the density. These relations were recently derived for SGT having temperature-dependent influence parameters by Magnanelli *et al.* [54], who we refer to for further information. For instance, the chemical potential is

$$\mu=\mu_{\rm eos}(\rho(\mathbf{r}),T)-\eta(T)\nabla^2\rho(\mathbf{r})-\frac{\partial\eta(T)}{\partial T}\nabla\rho(\mathbf{r})\cdot\nabla T(\mathbf{r}), \tag{13}$$

and the specific enthalpy is

$$\begin{aligned}h_{\rm sgm}(\rho(\mathbf{r}),T)=h_{\rm eos}(\rho(\mathbf{r}),T)&-\frac{T(\mathbf{r})}{2\rho(\mathbf{r})}\frac{\partial\eta(T)}{\partial T}|\nabla\rho(\mathbf{r})|^2\\&-\eta(T)\nabla^2\rho(\mathbf{r})-\frac{\partial\eta(T)}{\partial T}\nabla T(\mathbf{r})\cdot\nabla\rho(\mathbf{r}).\end{aligned} \tag{14}$$

Beyond equilibrium, we must also solve the balance equations for mass, energy, and momentum through the interface region. For a flat surface during steady-state evaporation and condensation, the balance equations reduce to a set of constant fluxes, J, J_m, and J_e, determined by the boundary conditions:

$$\rho v=J, \tag{15}$$

$$\rho v^2+p_\perp=J_m, \tag{16}$$

$$J_q'+J(h+0.5v^2)=J_e, \tag{17}$$

where J_m is the momentum flux and $p_\perp$ is the pressure perpendicular to the interface. Equivalent equations can be formulated for curvilinear geometries [26]. Moreover, the temperature follows from

$$\nabla\left(\frac{1}{T(\mathbf{r})}\right)=\mathbf{J}_q' r_{qq}(\mathbf{r}). \tag{18}$$

This implies that once an expression for the local resistivity r_{qq} is known, it is possible to numerically solve the coupled differential equations defining the SGT for a given set of boundary conditions, as elaborated in previous work [26]. For the flat interface, the solution gives the constants, J, J_m, and J_e, but also temperature and density profiles and all properties that depend on these. Hence, r_{qq} represents the missing piece in the nonequilibrium-SGT formulation. In the bulk regions, it is connected to the thermal conductivity λ through

$r_{qq} = (\lambda T^2)^{-1}$. The thermal conductivity of the bulk phases of water was in this work described by the state-of-the-art reference model [42]. For TIP4P/2005, we calculated the thermal conductivity of the bulk phases for each case as elaborated in Sec. II C [43] and report the values obtained in Table III in the Appendix. We found the following expression to describe well the magnitude and location of the temperature jump of water [25]:

$$r_{qq}(\mathbf{r}) = \frac{1}{\lambda(T,\rho)T(\mathbf{r})^2} + \frac{\beta(T^s)}{\rho(\mathbf{r})^4}|\nabla\rho(\mathbf{r})|^2. \quad (19)$$

We report the function $\beta(T^s)$ for water and TIP4P/2005 in Table II in the Appendix. While it is necessary to use nonequilibrium SGT to compare the density and temperature profiles to NEMD simulations, the interface transfer coefficients can be calculated from equilibrium solutions of SGT, using the integral relations. For the flat interface, the integral relations are [25]

$$R_{ij}(T,\xi) = \int_{-\infty}^{\infty} dz[\phi_{ij}(z)^{\text{ext}}], \quad (20)$$

where ξ is the position of the equimolar surface. Here, superscript ext means $\phi(z)^{\text{ext}} = \phi(r) - \phi^{\text{i}}\Theta(\xi - z) - \phi^{\text{o}}\Theta(z - \xi)$, where Θ is the Heaviside function. Equation (20) can be used to calculate the interface transfer coefficients with the arguments $\phi_{qq} = r_{qq}, \phi_{q\mu} = r_{qq}(h^{\text{o}} - h)$, and $\phi_{\mu\mu} = r_{qq}(h^{\text{o}} - h)^2$.

We shall next elaborate how to determine the curvature corrections in Eq. (3) d_{ij}, ν_{ij}, and $\overline{\nu}_{ij}$ using SGT. This is done most accurately by defining them analytically, following the procedure in Ref. [34]. We used the same methodology as described by Blokhuis and Bedeaux for the surface tension, and expanded the density and chemical potential of a spherical droplet (subscript s) in the inverse droplet radius, ξ^{-1} [60]:

$$\rho_s(z) = \rho_0(z) + \frac{1}{\xi}\rho_{s,1}(z) + \frac{1}{\xi^2}\rho_{s,2}(z) + \cdots, \quad (21)$$

$$\mu_s = \mu_0 + \frac{1}{\xi}\mu_{s,1} + \frac{1}{\xi^2}\mu_{s,2} + \cdots, \quad (22)$$

where $z = r - \xi$. We refer to the functions $\rho_0(z), \rho_{s,1}(z), \ldots$ as density expansion functions. The above equations can now be used in Eq. (13), where the Laplace operator is in spherical coordinates. By collecting terms of the same order, we obtain a set of second order coupled differential equations given in Refs. [34,61]. The procedure is repeated for a cylindrical geometry (subscript c). Solving these coupled differential equations determines the density expansion functions, i.e., $\rho_0(z), \rho_{s,1}(z), \rho_{s,2}(z)$ and $\rho_{c,1}(z), \rho_{c,2}(z)$, and their corresponding spatial derivatives. We must also define the curvature expansion functions of the enthalpy and the local resistivity:

$$h_s(z) = h_0(z) + \frac{1}{\xi}h_{s,1}(z) + \frac{1}{\xi^2}h_{s,2}(z) + \cdots, \quad (23)$$

$$r_{qq,s}(z) = r_{qq(0)}(z) + \frac{1}{\xi}r_{qq(s,1)}(z) + \frac{1}{\xi^2}r_{qq(s,2)}(z) + \cdots, \quad (24)$$

and equivalently for the cylindrical geometry. Once the density expansion functions are known for a spherical and cylindrical geometry, respectively, the curvature corrections in Eq. (3) can be obtained as functions of temperature by following the same procedure as in Ref. [34]. We refer to the Appendix of Ref. [34] for the analytic expressions for d_{ij}, ν_{ij}, and $\overline{\nu}_{ij}$ in terms of the density expansion functions as well as further details about the derivations.

III. THE RESULTS

In the following, we shall obtain the coefficients to describe transport of heat and mass across flat and curved vapor-liquid interfaces of water with Eqs. (1)–(3). First, we discuss the ability of the tools we have used to represent the properties of real water (Sec. III A). The interface transfer coefficients of the planar interface are evaluated at low temperatures utilizing the available water-evaporation experiments (Sec. III B), and at high temperatures using NEMD (Sec. III C). We then evaluate the interface transfer coefficients along the whole coexistence line by combining experiment results, NEMD and SGT (Sec. III D), before we present and evaluate the curvature corrections (Sec. III E). Finally, we give a brief discussion on how the results presented can be used to improve current climate models (Sec. III F).

A. Comparing the tools

Figure 4 shows the density [Fig. 4(a)] and the surface tension [Fig. 4(b)] along the vapor-liquid coexistence line of

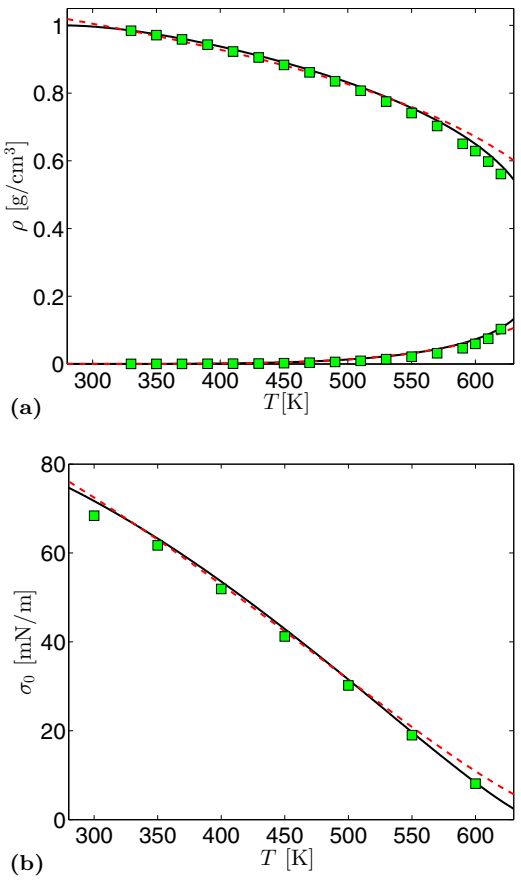

FIG. 4. The coexistence densities (a) and the surface tension (b), from experiments (solid lines), SGT (red dashed line), and TIP4P/2005 (green squares) [37,63].

water, where both SGT (red dashed line) and the TIP4P/2005 model (green squares) give properties very close to real water (solid line). While the CPA equation of state for water is within the experimental accuracy for the saturation pressure, it is underpredicted by the TIP4P/2005 model. Vega and Abascal argued that it might be necessary to include polarizability to capture the saturation pressure accurately [62]. Other properties such as the vaporization enthalpy are reproduced well by both models, suggesting that they are capable of predicting properties not explicitly used in their fitting procedures. Also nonequilibrium properties are predicted to a good accuracy by the TIP4P/2005 model. For instance, the thermal conductivity predicted for liquid-phase water at high temperatures deviates only 10% from experiments [43]. Moreover, TIP4P/2005 predicts the anomalous thermal conductivity maximum observed experimentally, hence confirming that the model reproduces the anomalous behavior of water [43]. In SGT, we employ the state-of-the-art empirical model for the thermal conductivity of the bulk-phases and reproduce, by construction, the thermal conductivity of water within the experimental accuracy [42]. Since both SGT and the TIP4P/2005 model give properties similar to real water, we are confident that they also provide realistic predictions of the interface transfer coefficients, as we will discuss further in Sec. III D.

B. Low temperatures

The water-evaporation experiments by Badam *et al.* [21] combined with SGT give the possibility to calculate the interface transfer coefficients for water in the interval ∼260–280 K. We will show that the experimental results can be rationalized within the framework of nonequilibrium thermodynamics.

The data which underlie the present analysis come from 45 independent experiments, where the pressure and heating rate of the vapor phase have been changed systematically (see Table IV in the Appendix). The temperature was measured at spatial positions along a center line perpendicular to the interface, going from the vapor phase to the liquid phase, giving temperature measurements as plotted in Fig. 5(a). The heat fluxes in both phases were calculated based on the temperature gradients as elaborated in Sec. II B. Moreover, we followed the procedure outlined in NET and extrapolated the relevant quantities to the dividing surface, indicated by the vertical solid line in Fig. 5(a). The figure shows a jump in temperature across the interface, due to the interfacial resistance. The magnitude of the jump depends on the experimental conditions, and has been plotted for all 45 experiments in Fig. 5(b) (red squares).

According to NET, the interface transfer coefficients across the flat interface depend on the interface temperature, T^s. For all the experiments, T^s equals T^l to a very good accuracy, as discussed in Sec. II A.

As an initial approach to get a notion of the magnitude and temperature dependence of the interface transfer coefficients, we approximated $R_{qq,0}$ and $R_{q\mu,0}$ as linear functions of T^l. Using an optimization routine, we identified the coefficients which minimized the least squares norm between the experimental temperature jumps and those obtained using Eq. (1) from Sec. II A. Since the interface transfer coefficients are nonlinear functions of the temperature, the optimized linear functions are of little use outside the experimental temperature

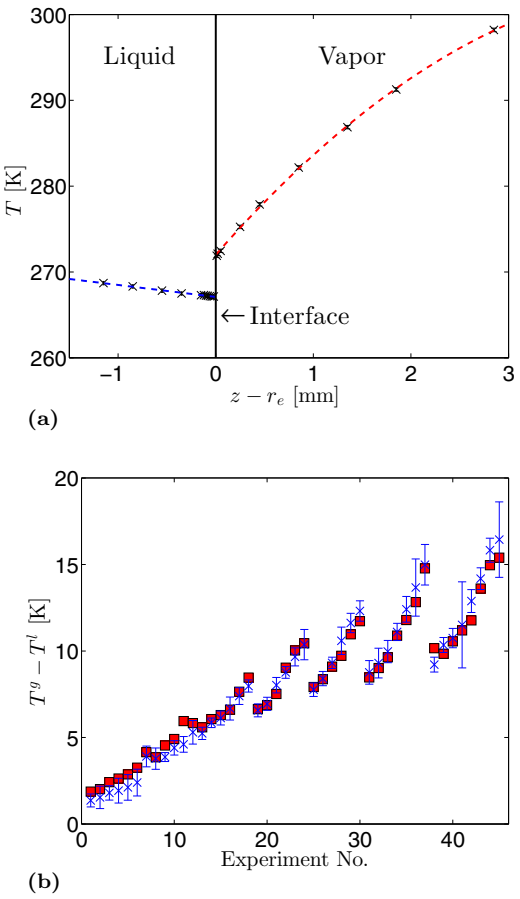

FIG. 5. Temperature measurements (a) from experiment No. 10. Panel (b) shows the interface temperature jumps from the experiments (red squares) and SGT (blue crosses). Details for each experiment can be found in Table IV in the Appendix.

range. However, what we learned was that the heat of transfer, q^*, should be less than 5% of the enthalpy of vaporization to comply with experimental results. In the SGT formulation, this means that the second term on the right-hand side of Eq. (19) should depend on $\rho(\mathbf{r})$ as $\rho(\mathbf{r})^{-n}$ where $n \geqslant 4$. We found that SGT using $n = 4$ in Eq. (19) matched well with both experiments and simulations. Further, the prefactor, $\beta(T^s)$, of Eq. (19) depended exponentially on T^s [as shown in Eq. (A1) in the Appendix]. We used the 20 most accurate experiments from Badam *et al.* [21] to estimate this exponential function, with coefficients reported in Table II in the Appendix.

All the interface transfer coefficients can then be calculated with SGT, and they follow the solid lines in Fig. 6. The red squares in Fig. 6(a) represent the value of $R_{qq,0}$, estimated from the data from each experiment. Some of the estimates have large error bars. In particular, the first 6 experiments have very small temperature gradients in the vapor phase, and hence a large uncertainty in the calculated heat fluxes. Nonetheless, the $R_{qq,0}$ from SGT (solid line) was within the uncertainty of most of the experiments (red squares).

As shown in Fig. 6(d), the coupling between heat and mass transfer, represented by the heat of transfer, amounts to less than 4% of the enthalpy of vaporization, in agreement with the initial optimization procedure. This is also in agreement

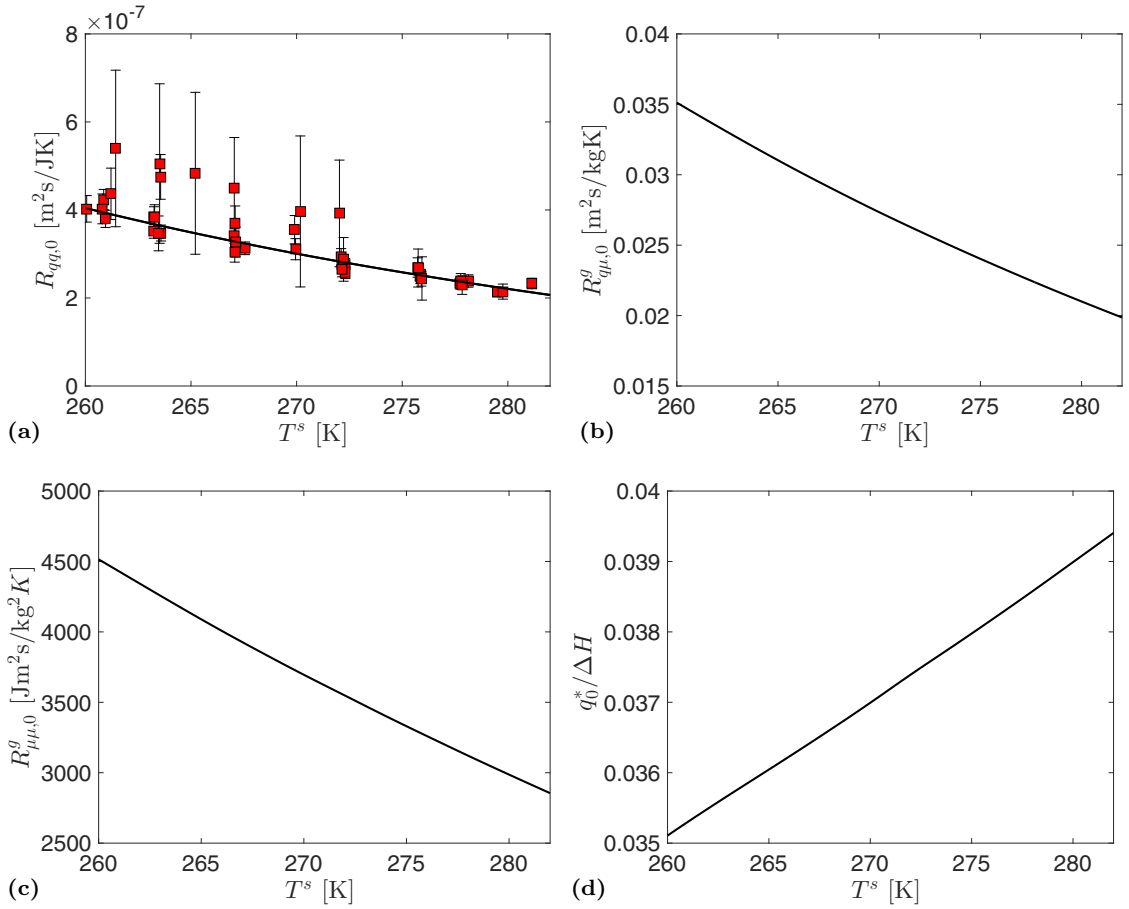

FIG. 6. Interface transfer coefficients from experiments (red squares) and from SGT (solid lines). Panel (d) shows the heat of transfer divided by the vaporization enthalpy. $R_{qq,0}$ for each experiment can be found in Table IV in the Appendix.

with previous work dealing with the Lennard-Jones fluid, which showed that the coupling was less pronounced at low temperatures (see Fig. 8 in Ref. [34]).

The coefficients $R_{qq,0}(T^s)$ and $R_{q\mu,0}(T^s)$ can now be used to predict the temperature jump for each experiment, using Eq. (1) from Sec. II A, where the right-hand side requires only the vapor-phase heat flux, the mass flux, and the liquid-phase temperature as input. The blue crosses in Fig. 5(b) show that most of the predicted temperature jumps agree with the experimental results within their uncertainty.

Since $R_{qq,0}(T^s)$ and $R_{q\mu,0}(T^s)$ from SGT clearly are capable of reproducing the experimental temperature jumps, an important next question is whether $R_{\mu q,0}$ and $R_{\mu\mu,0}$ from SGT can reproduce the evaporation rates from the experiments. We found that the pressures measured in the vapor phase by Badam *et al.* [21] were arbitrarily scattered around the saturation pressure within the uncertainty of the experimental facility (±13 Pa). Unfortunately, this meant that they had too much uncertainty to provide an independent assessment of $R_{\mu\mu,0}$.

The ability of SGT to reproduce the experimental mass flux was evaluated with the nonequilibrium square gradient model [54], using the conditions from the experiments as boundary conditions. We considered a simulation volume where the interface was positioned in the middle, with liquid to the left and vapor to the right. Further, we imposed the temperatures T^l and T^g as boundary conditions and identified the pressure at the vapor side, which reproduced the experimental mass flux from Table IV in the Appendix. A perfectly flat interface was considered since the interfacial curvature in these experiments is too low to influence the magnitude of the interface transfer coefficients. Nonequilibrium SGT predicted that the pressure of the vapor phase was less than 10 Pa away from the pressure of the liquid phase. This is consistent with the experimental results within their accuracy, and states that the interface is in mechanical equilibrium. The interface is indeed in mechanical equilibrium during the experiments, since its position changes less than ±10 μm. The driving force for evaporation when steady state has been reached is thus the large difference in temperature.

We report the heat fluxes predicted from nonequilibrium SGT in Fig. 7 (blue crosses). The liquid-phase heat flux deviates on average 3% from the corresponding estimates from the experiments, while the vapor-phase heat flux deviates on average 8% from the experimental results. For most of the experiments, SGT was able to reproduce the estimated heat flux within the experimental uncertainty.

The results from Fig. 7 can also be interpreted in another way. Imposing as a boundary condition in the nonequilibrium square gradient model the heat flux in the liquid phase from Fig. 7(a) or the heat flux in the vapor phase from Fig. 7(b), which are within 10% of the experimental predictions, would

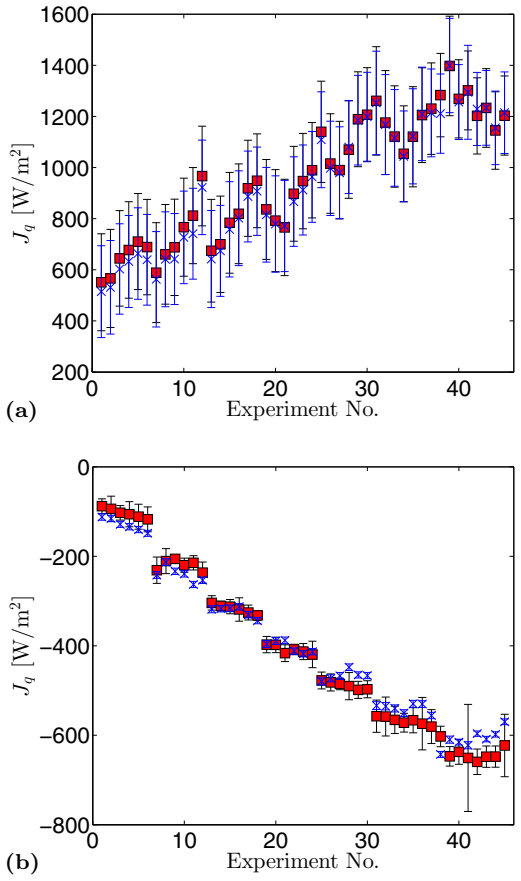

FIG. 7. The heat flux in the liquid phase (a) and vapor phase (b), from experiments (red squares) and from nonequilibrium SGT (blue crosses). Details for each experiment can be found in Table IV in the Appendix.

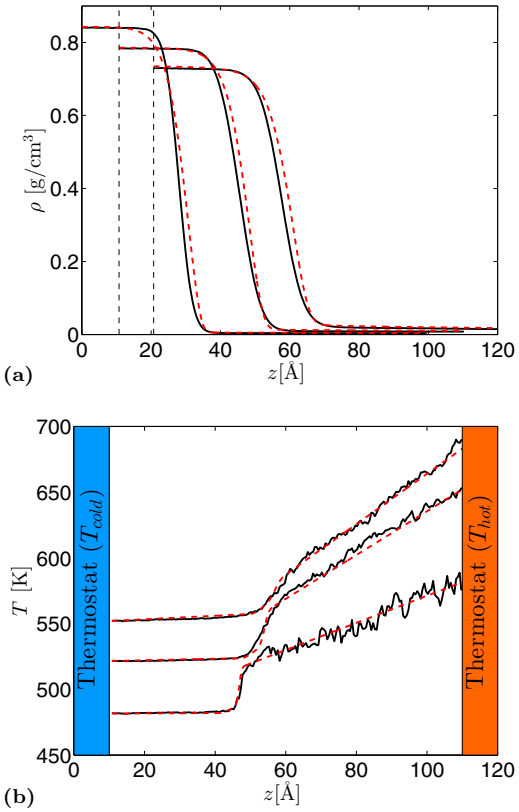

FIG. 8. Density profiles (a) and temperature profiles (b) from NEMD (solid lines) and nonequilibrium SGT (red dashed lines), where the density profiles have been shifted to the vertical dashed lines for readability.

reproduce the mass flux from the experiments. This clearly illustrates that SGT is capable of describing the characteristics of the interface to a very good accuracy, and that $R_{\mu\mu,0}$ from SGT is trustworthy.

C. High temperatures

The interface transfer coefficients decrease exponentially with increasing temperature and approach zero at the critical point [34]. At high temperatures, they cannot be measured experimentally, as the temperature jump becomes too small.

However, the interface transfer coefficients can be calculated by combining NEMD simulations with SGT as explained in Sec. II C. We stated in previous work that it was crucial to use an accurate equation of state to obtain reliable results with SGT [64]. To represent the interface of TIP4P/2005 as accurately as possible, we developed the TIP4P/2005-CPA equation of state as elaborated in the Appendix, and coupled this to SGT.

In Fig. 8, we compare nonequilibrium SGT to NEMD simulations, using the parameters given in Table II in the Appendix. The figure shows that both the bulk-phase densities and the density across the interface from NEMD are reproduced to a good accuracy by nonequilibrium SGT. Moreover, Fig. 8(b) shows that nonequilibrium SGT also reproduces both the location and the magnitude of the temperature jump from NEMD simulations, hence capturing the behavior of the interface beyond equilibrium.

Figure 9 presents the interface transfer coefficients in the interval $T^s = 480$–560 K. The green squares come from NEMD simulations, using the prescription outlined in Sec. II C. They compare very well with results from SGT (solid line). Since the temperature and density profiles from nonequilibrium SGT coincide with results from NEMD as shown in Fig. 8, the Soret equilibrium established in the simulation cell gives that also the coefficient $R_{q\mu,0}$ is the same for the two methodologies [set $J = 0$ in Eq. (2)]. We have reported details from the NEMD simulations in Table V in the Appendix. In the NEMD simulations, the liquid-phase thermostat was changed in intervals of 10 K from 480 K to 550 K. We calculated the surface temperature using nonequilibrium SGT and the following relation, which is true only for the equimolar dividing surface [53]:

$$T^s = h^s/s^s, \tag{25}$$

where h^s and s^s are the excess enthalpy and entropy, respectively. For all the cases considered, we find that $T^s \simeq T^l$. The liquid-phase temperatures as well as the interface temperatures have been reported in Table V in the Appendix for comparison.

D. The overall picture

SGT was in Sec. III B fitted to match experimental data, and in Sec. III C to match results from NEMD. As discussed in Sec. III A, the properties of TIP4P/2005 deviate from those

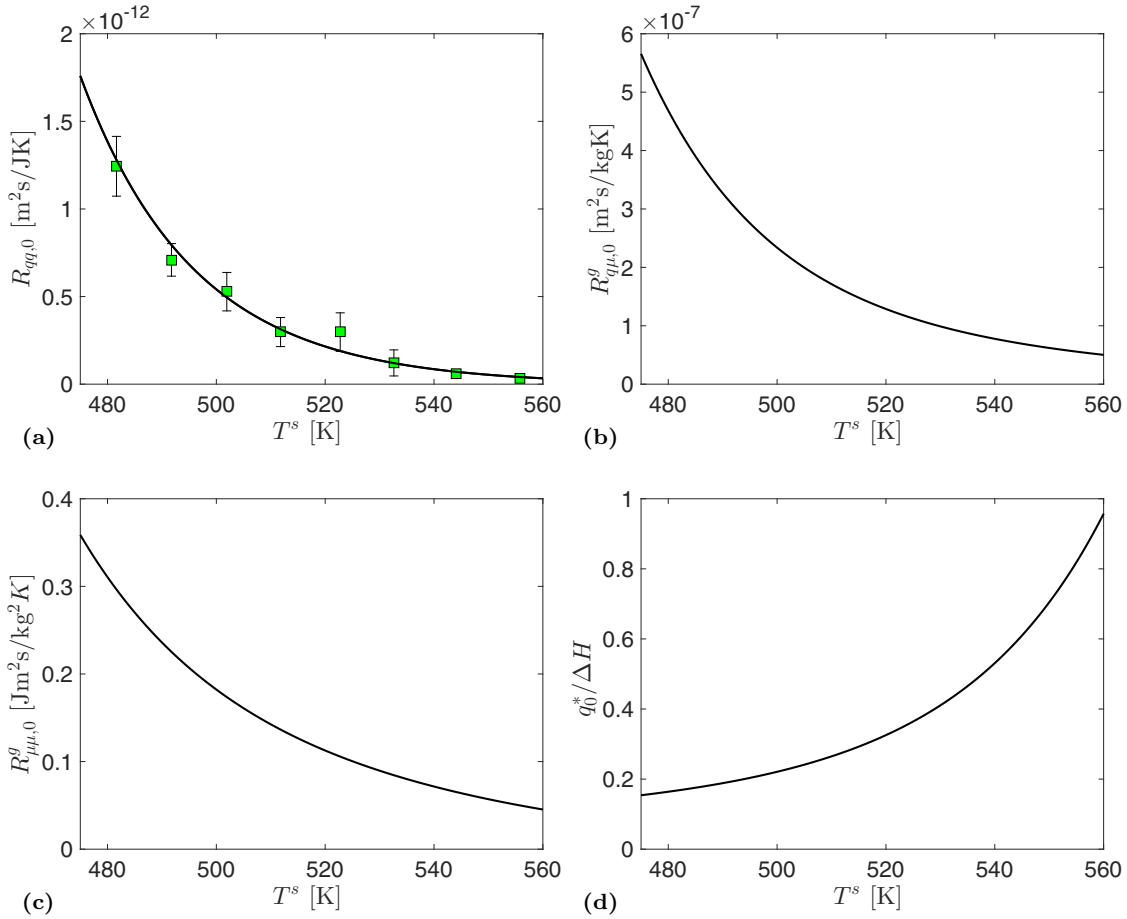

FIG. 9. Interface transfer coefficients from NEMD (green squares) and from SGT (solid lines). Panel (d) shows the heat of transfer divided by the vaporization enthalpy. Additional results from the simulations can be found in Table V in the Appendix.

of real water. Moreover, there is a considerable range in temperature (280 K to 480 K) where data from experiments and simulations are unavailable.

Figure 10 presents the interface transfer coefficients in the range 260 K to 550 K, where SGT has been extrapolated beyond the range where its coefficients have been fitted (dashed lines). The figure shows that all interface transfer coefficients, whether they have been extrapolated from real water at low temperatures or from TIP4P/2005 at high temperatures, approach each other. This strongly suggests that TIP4P/2005 gives interface transfer coefficients similar to those of real water, and that it is possible to represent the interface transfer coefficients along the whole vapor-liquid coexistence line, taking advantage of both experiments and simulations.

We found the $\beta(T^s)$ function for which SGT reproduced temperature jumps from both experiments and simulations, resulting in the blue dash-dotted line in Fig. 10. Since the enthalpy of TIP4P/2005 deviates slightly from that of real water, the solid lines also deviate slightly from the blue dash-dotted lines at high temperatures for all the coefficients except $R_{qq,0}$. This can be explained on the basis of the integral relations introduced in Sec. II D, where the expressions for $R_{q\mu,0}$ and $R_{\mu\mu,0}$ have contributions from the enthalpy. All the coefficients $R_{qq,0}, R_{q\mu,0}, R_{\mu\mu,0}$ have been tabulated in the Supplemental Material [65].

In the range 280 K to 480 K, there are currently no experimental data or simulation results available. Such results could be useful to evaluate the accuracy of the interface transfer coefficients from SGT (blue dash-dotted lines in Fig. 10). Several approaches can be attempted in the future to explore the interface transfer coefficients of water in this region. One possibility is to use less computationally demanding water models [48]. Another possibility is to take advantage of the transient relaxation to equilibrium, following a similar approach to that of Lervik *et al.* [66], or to utilize Green-Kubo relations in combination with equilibrium simulations similarly to Refs. [67–69].

E. The curvature corrections

A major benefit of mapping the heat transfer characteristics from the experiments and the simulations onto the SGT description is that SGT can then be used to predict their curvature dependence (see Sec. II D). In Fig. 11 we have plotted the first and second order curvature corrections defined in Eq. (3). The first order corrections, d_{ij}, have the same dimension as the leading order curvature correction of the surface tension, the Tolman length. The Tolman length of water was recently found to be about -0.05 nm at 300 K [7,70], i.e., about 35 times smaller than the first order corrections

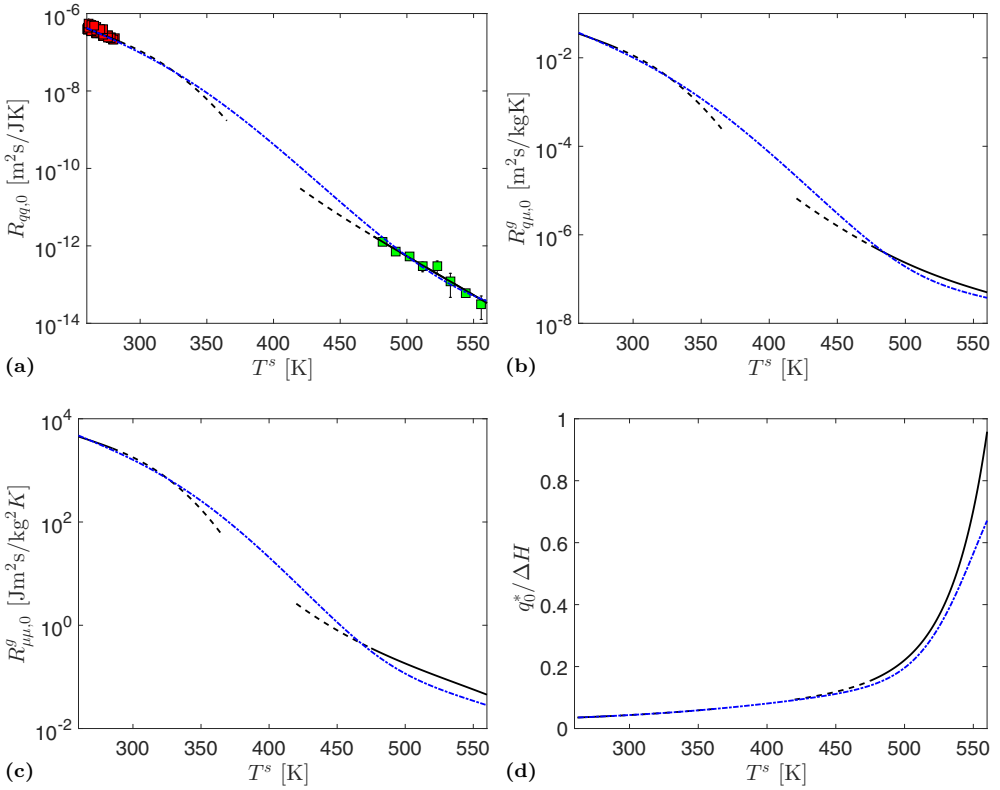

FIG. 10. Interface transfer coefficients from experiments (red squares), NEMD (green squares), SGT (solid lines), extrapolation of SGT (dashed lines), and SGT fitted to match both experiments and NEMD (blue dash-dotted line). Panel (d) shows the heat of transfer divided by the vaporization enthalpy.

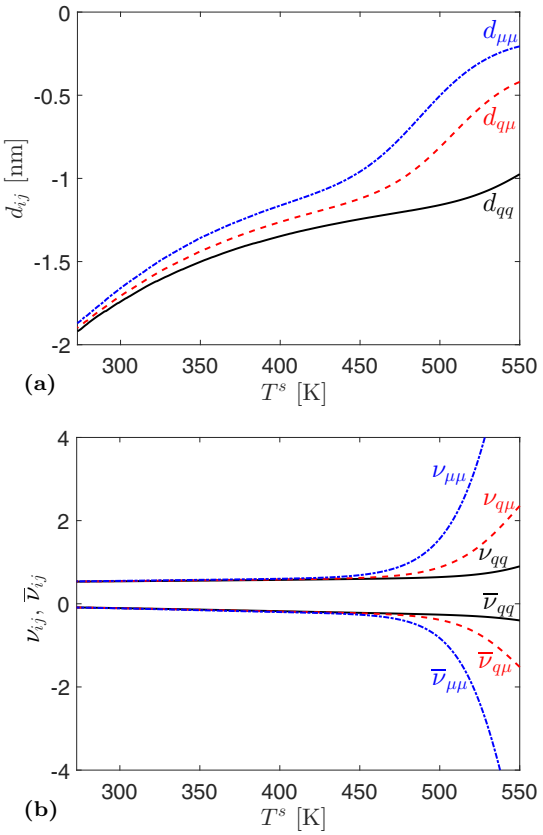

FIG. 11. The first and second order curvature corrections of the interface transfer coefficients of water.

presented in Fig. 11. Curvature has thus a more dramatic effect on transport across the water interface than on the surface tension. While the magnitude of the first order corrections decays with temperature, the second order terms are nearly independent of temperature, $\nu_{ij} \sim 0.54$ and $\overline{\nu}_{ij} \sim -0.09$, until $T = 450$ K, where enthalpic contributions start to enhance their magnitudes.

We can evaluate the correctness of the coefficients d_{ij}, ν_{ij}, and $\bar{\nu}_{ij}$ and the range of validity of the second order curvature expansion by comparing the curvature expansion to results from using solutions of the SGT at equilibrium for a spherical and cylindrical geometry in combination with the integral relations (see also Refs. [25,34]). While the integral relations can be used for spherical and cylindrical geometries, we emphasize that only the curvature expansion in Eq. (3) can handle heat and mass transfer through interfaces of more complex geometries such as the interfaces of coalescing nanodroplets.

Figure 12 shows that the curvature influences bubbles (negative curvature) more than droplets (positive curvature). Moreover, at 300 K, the figure shows that the second order curvature expansion (dashed lines) reproduces accurately the results from the integral relations (solid lines) until a total curvature of about ± 0.4 nm^{-1}, which corresponds to spherical droplets/bubbles with radii of 5 nm, and cylindrical droplets/bubbles with radii of 2.5 nm. Figure 12 thus confirms the validity of the curvature corrections presented in Fig. 11. All the curvature corrections have been tabulated in the Supplemental Material [65].

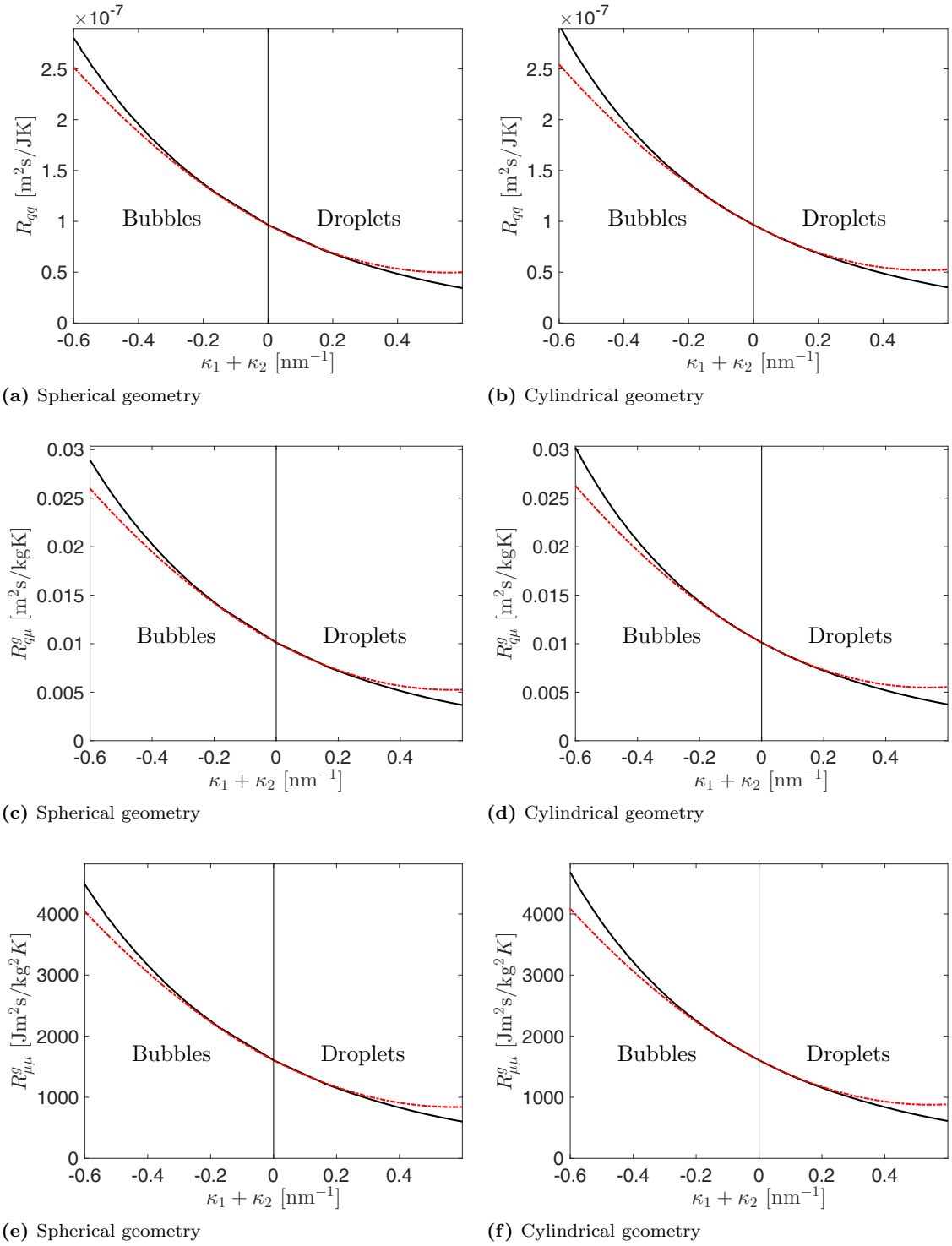

(a) Spherical geometry **(b)** Cylindrical geometry

(c) Spherical geometry **(d)** Cylindrical geometry

(e) Spherical geometry **(f)** Cylindrical geometry

FIG. 12. The interface transfer coefficients calculated with square-gradient theory and the integral relations (solid lines), and with the curvature expansion (red dashed lines), for spherical and cylindrical bubbles and droplets. The results are for water at $T = 300$ K.

F. From nanodroplets to climate models

We have in this work obtained the temperature and curvature dependence of the interface transfer coefficients of water. They have a wide range of applications, and we shall discuss one central example in particular: their role in climate models. We emphasize, however, that the results presented apply to many other industrial or natural phenomena.

The CCSM4 climate model predicts a scenario where all the summer ice has disappeared from the Arctic in only 80 years due to global warming [71]. Such a scenario has dramatic global consequences. However, there is today a large uncertainty connected with precipitation and circulation of water [10]. This is no surprise, since these phenomena have been handled by fitting empirical correlations to a selection of experimental data [71,72]. The fundamental physical

description has been lacking. This is where the framework and coefficients in this work can contribute.

To describe water evaporation from oceans and lakes, the two most significant contributions come from the resistances to heat and mass transfer of the water interface and the resistances associated with a thin layer of air just above the ocean surface. The resistances of the planar water interface, $R_{ij,0}$, are tabulated in this work [65]. The resistances of the boundary layer depend on wind conditions and can be obtained using boundary-layer theory [73]. The resistances of the interface and the boundary layer can next be combined, using the principle of "resistances in series," in analogy with electrical circuits [74]. This opens the route to improve the accuracy and predictive ability of the crude empirical relations used to describe evaporation, for instance in the CCSM4 climate model [71] (see Sec. 4.10 in Ref. [72] for details).

After water evaporates, droplets form clouds in the atmosphere via heterogeneous nucleation. The droplets increase their volumes by orders of magnitude before eventually precipitating as rain and completing the water cycle. Small droplets grow primarily by depleting the atmospheric water vapor, and the magnitude of the interface transfer coefficients R_{ij} determines their growth rates. Since water droplets are close to spherical, their growth rates can be predicted by particularizing Eq. (3) for a spherical geometry: $H = 2/\xi$ and $K = 1/\xi^2$, where ξ is the droplet radius. Figure 12 shows that the interface transfer coefficients vary significantly with the droplet radius for nanosized droplets. This makes the curvature corrections important for improving the parametrizations used to describe the rate of cloud formation and precipitation in current climate models (see Sec. 4.5 in Ref. [72] for details).

IV. CONCLUSION

The main achievement of this work has been to provide a complete set of coefficients to coherently describe transport of heat and mass across planar and curved vapor-liquid interfaces of water from 260 to 560 K, using the framework of nonequilibrium thermodynamics. To achieve this, we used water-evaporation experiments at low temperatures and nonequilibrium molecular dynamics with the TIP4P/2005 model at high temperatures to calibrate square gradient theory. Square gradient theory was then used to calculate all the interface transfer coefficients along the coexistence line as well as their curvature corrections. We found in all cases that square gradient theory was capable of capturing the nonequilibrium properties of the interface, given that an appropriate equation of state and local resistivity functions were used.

The description has great practical relevance since it gives the possibility to accurately describe evaporation and condensation in large-scale systems such as climate models or in small-scale systems such as during evaporation or condensation of nanodroplets. The tools presented here can be further taken advantage of to study other water structures such as droplets or bubbles on solid surfaces [75–77], evaporation-driven engines [78], nanofluidic transport [79], or the odd-shaped water structures recently observed during supersonic nozzle experiments [80].

ACKNOWLEDGMENTS

We thank Dr. T. Furevik and Dr. I. Bethke at the Bjerknes Centre for Climate Research for sending the documentation on their climate models. This research was supported in part with computational resources at NTNU provided by NOTUR [81]. A.L. thanks the Research Council of Norway (RCN) for financial support.

APPENDIX: SUPPLEMENTARY INFORMATION

In this Appendix, we have included details about the TIP4P-CPA equation of state (Sec. A 1), the parameters used in the local resistivity of SGT (Sec. A 2), and details from the experiments and simulations (Sec. A 3). To estimate the error propagation, we have used the conventional variance formula.

1. The TIP4P-CPA equation of state

We refer to Queimada *et al.* for the exact mathematical formulation of the CPA equation of state used in this work [57]. The equation of state relies on 5 parameters: a_0,b,c_1,β, and ϵ, where the first three are associated with the cubic part, and the last two with the association part of the equation of state. Moreover, to precisely predict the temperature dependence of the surface tension of water, the influence parameter was formulated by Queimada *et al.* as a function of temperature, using the three parameters D, E, and F. The parameters which best represent real water were given by Queimada *et al.* [57]. We obtained them also for TIP4P/2005, by first minimizing the mean square deviation between the equation of state and the data by Vega *et al.* [37] for the first five parameters, and then minimizing the deviation between the surface tension from square gradient theory and the surface tension for TIP4P/2005 given by Alejandre *et al.* [63] to obtain the parameters E and F. The minimization procedure was carried out repeatedly using several different algorithms to ensure that the fit was as good as possible. The parameters we obtained are listed in Table I, where we have used the same nomenclature as Queimada *et al.* Employing these coefficients gives the coexistence densities and the saturation pressure presented in Fig. 13 and the surface tension reported in Fig. 14. The figures show that the fitted equation of state matches very well with the data, and the mean deviation is for all properties below 3% and within the computational error.

TABLE I. The parameters used in the TIP4P/2005 equation of state, and the corresponding SGT formulation. We used the same nomenclature as Ref. [57], which we refer to for further information.

Symbol	Value	Units
a_0	0.0184	J m^3/mol^2
b	1.3×10^{-5}	m^2/mol
c_1	3	
β	0.0802	
ϵ	20.48	kJ
D	14.73	
E	−12.49	
F	−7.30	

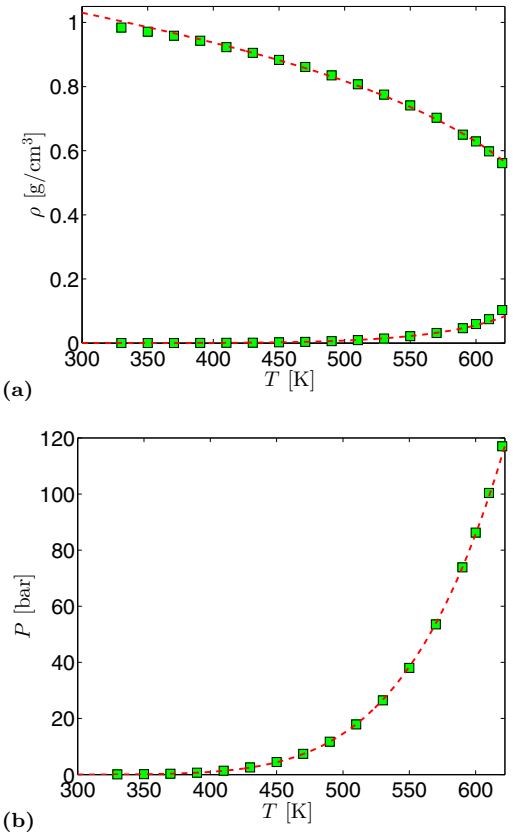

FIG. 13. The coexistence densities (a) and saturation pressure (b) of TIP4P/2005 [37] (green squares) and the TIP4P/2005 CPA equation of state (red dashed lines).

2. The local resistivity in SGT

In the local resistivity of the SGT formulation in Sec. II B, the parameter $\beta(T^s)$ was used, where T^s is the temperature of the interface. By plotting the interface resistivities normalized by the predictions from SGT in a semilogarithmic plot, we saw that the prefactor, $\beta(T^s)$, was an exponential function,

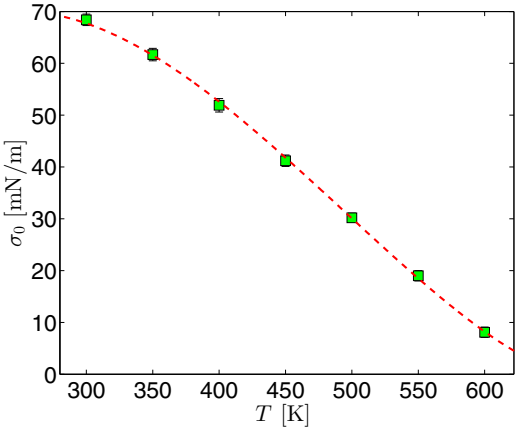

FIG. 14. Surface tensions from simulations (green squares) [63] and from the TIP4P/CPA equation of state coupled with SGT (red dashed line).

TABLE II. The parameters used in the local resistivity function of SGT (SI units).

Case		γ_1	γ_2	γ_3	γ_4
Low T	(Sec. III B)	0.00	-7.71×10^{-4}	0.56	−137.9
High T	(Sec. III C)	0.00	-5.30×10^{-5}	0.06	−55.6
All T	(Sec. III D)	1.23×10^{-6}	-1.74×10^{-3}	0.81	−158.4

where

$$\ln[\beta(T^s)] = \gamma_1(T^s)^3 + \gamma_2(T^s)^2 + \gamma_3 T^s + \gamma_4. \quad \text{(A1)}$$

To represent the interfacial resistance at low temperatures or at high temperatures only, it was sufficient to use a quadratic polynomial as stated by the first two rows of Table II. However, to represent the whole range of temperatures, we had to use a third order polynomial. The coefficients used have been reported in Table II. Moreover, the thermal conductivities used in the bulk phases when addressing TIP4P/2005 with SGT have been reported in Table III. The thermal conductivity of the liquid phase can readily be compared to the value along the coexistence line for real water [42], which TIP4P/2005 overpredicts by 25% on average in the interval 480 K to 550 K, where the agreement is better at higher temperatures.

The thermal conductivity of the vapor phase in Table III is not easily compared to the thermal conductivities at saturation for real water, since the vapor phase is ∼100 K higher than the saturation temperature. Moreover, the saturation pressure of TIP4P/2005 deviates from that of real water, as discussed in Sec. III A, which we refer to for further discussion of the TIP4P/2005 model.

3. Details from the experiments and simulations

We have reported results from the experiments with the associated uncertainty in Table IV, and similarly for the simulations in Table V. The surface temperature in Table V has been estimated from SGT, and is very similar to the liquid-phase temperature for all the cases considered. We observe that the surface temperature starts to deviate from the liquid-phase temperature by more than 1 K, when $\rho^l/\rho_g < 50$.

TABLE III. The thermal conductivities of TIP4P/2005 from the NEMD cases in Sec. III C.

T^{cold} (K)	T^{hot} (K)	λ^{liq} (W/mK)	λ^{gas} (W/mK)
480	630	0.882	0.009
490	640	0.826	0.015
500	650	0.830	0.023
510	660	0.801	0.027
520	670	0.773	0.027
530	680	0.767	0.031
540	690	0.706	0.038
550	700	0.659	0.046

TABLE IV. Results from the water-evaporation experiments by Badam *et al.* [21]. A value for $R_{qq,0}$ has been calculated from the experimental data at each experiment, using $R_{q\mu,0}$ from SGT.

Expt. No.	T^g (K)	T^l (K)	$J_q'^g$ (W/m^2)	$J_q'^l$ (W/m^2)	J (kg/s m^2)	$R_{qq,0}$ (m^2 s/J K)
1	273.9± 0.1	272.0± 0.1	−88 ± 16	551± 190	$2.5 \times 10^{-4} \pm 8 \times 10^{-5}$	$3.9 \times 10^{-7} \pm 1.2 \times 10^{-7}$
2	272.2 ± 0.1	270.2 ± 0.1	−94± 28	566 ± 192	$2.6 \times 10^{-4} \pm 8 \times 10^{-5}$	$4.0 \times 10^{-7} \pm 1.7 \times 10^{-7}$
3	269.5 ± 0.1	267.0 ± 0.1	−103 ± 16	645 ± 187	$3.0 \times 10^{-4} \pm 7 \times 10^{-5}$	$4.5 \times 10^{-7} \pm 1.2 \times 10^{-7}$
4	267.8 ± 0.1	265.2 ± 0.1	−106 ± 28	678 ± 189	$3.1 \times 10^{-4} \pm 8 \times 10^{-5}$	$4.8 \times 10^{-7} \pm 1.8 \times 10^{-7}$
5	266.4 ± 0.1	263.5 ± 0.1	−111 ± 28	710 ± 188	$3.2 \times 10^{-4} \pm 8 \times 10^{-5}$	$5.1 \times 10^{-7} \pm 1.8 \times 10^{-7}$
6	264.7 ± 0.1	261.4 ± 0.1	−117 ± 28	689 ± 186	$3.2 \times 10^{-4} \pm 7 \times 10^{-5}$	$5.4 \times 10^{-7} \pm 1.8 \times 10^{-7}$
7	279.9 ± 0.1	275.8 ± 0.1	−231 ± 29	589 ± 196	$3.3 \times 10^{-4} \pm 8 \times 10^{-5}$	$2.7 \times 10^{-7} \pm 4 \times 10^{-8}$
8	276.1 ± 0.1	272.2 ± 0.1	−211 ± 28	660 ± 195	$3.5 \times 10^{-4} \pm 8 \times 10^{-5}$	$2.9 \times 10^{-7} \pm 5 \times 10^{-8}$
9	274.4 ± 0.1	269.9 ± 0.1	−206 ± 9	688 ± 189	$3.6 \times 10^{-4} \pm 8 \times 10^{-5}$	$3.6 \times 10^{-7} \pm 3 \times 10^{-8}$
10	272.0 ± 0.1	267.1 ± 0.1	−220 ± 16	767 ± 192	$3.9 \times 10^{-4} \pm 8 \times 10^{-5}$	$3.7 \times 10^{-7} \pm 4 \times 10^{-8}$
11	269.5 ± 0.1	263.6 ± 0.1	−215 ± 16	812 ± 188	$4.0 \times 10^{-4} \pm 7 \times 10^{-5}$	$4.8 \times 10^{-7} \pm 5 \times 10^{-8}$
12	267.0 ± 0.1	261.2 ± 0.1	−236 ± 24	967 ± 195	$4.7 \times 10^{-4} \pm 8 \times 10^{-5}$	$4.4 \times 10^{-7} \pm 6 \times 10^{-8}$
13	281.3 ± 0.1	275.7 ± 0.1	−304 ± 16	674 ± 201	$3.9 \times 10^{-4} \pm 8 \times 10^{-5}$	$2.7 \times 10^{-7} \pm 2 \times 10^{-8}$
14	278.2 ± 0.1	272.1 ± 0.1	−311 ± 11	700 ± 188	$4.0 \times 10^{-4} \pm 8 \times 10^{-5}$	$2.9 \times 10^{-7} \pm 2 \times 10^{-8}$
15	276.2 ± 0.1	270.0 ± 0.1	−313 ± 16	784 ± 197	$4.4 \times 10^{-4} \pm 8 \times 10^{-5}$	$3.1 \times 10^{-7} \pm 2 \times 10^{-8}$
16	273.7 ± 0.1	267.1 ± 0.1	−319 ± 26	819 ± 195	$4.5 \times 10^{-4} \pm 8 \times 10^{-5}$	$3.3 \times 10^{-7} \pm 3 \times 10^{-8}$
17	270.9 ± 0.1	263.3 ± 0.1	−326 ± 17	919 ± 188	$4.9 \times 10^{-4} \pm 7 \times 10^{-5}$	$3.8 \times 10^{-7} \pm 3 \times 10^{-8}$
18	269.3 ± 0.1	260.9 ± 0.1	−332 ± 11	948 ± 183	$5.0 \times 10^{-4} \pm 7 \times 10^{-5}$	$4.2 \times 10^{-7} \pm 2 \times 10^{-8}$
19	284.4 ± 0.1	277.8 ± 0.1	−397 ± 18	836 ± 196	$4.9 \times 10^{-4} \pm 8 \times 10^{-5}$	$2.4 \times 10^{-7} \pm 2 \times 10^{-8}$
20	282.7 ± 0.1	275.9 ± 0.1	−398 ± 17	792 ± 199	$4.7 \times 10^{-4} \pm 8 \times 10^{-5}$	$2.5 \times 10^{-7} \pm 2 \times 10^{-8}$
21	279.7 ± 0.1	272.1 ± 0.1	−417 ± 19	766 ± 189	$4.7 \times 10^{-4} \pm 8 \times 10^{-5}$	$2.7 \times 10^{-7} \pm 2 \times 10^{-8}$
22	276.1 ± 0.1	267.1 ± 0.1	−408 ± 12	898 ± 186	$5.2 \times 10^{-4} \pm 7 \times 10^{-5}$	$3.4 \times 10^{-7} \pm 2 \times 10^{-8}$
23	273.3 ± 0.1	263.3 ± 0.1	−413 ± 18	947 ± 186	$5.3 \times 10^{-4} \pm 7 \times 10^{-5}$	$3.8 \times 10^{-7} \pm 2 \times 10^{-8}$
24	271.3 ± 0.1	260.8 ± 0.1	−419 ± 30	989 ± 187	$5.5 \times 10^{-4} \pm 7 \times 10^{-5}$	$4.0 \times 10^{-7} \pm 3 \times 10^{-8}$
25	286.1 ±0.1	278.1 ±0.1	−478 ± 19	1140 ± 198	$6.5 \times 10^{-4} \pm 8 \times 10^{-5}$	$2.4 \times 10^{-7} \pm 1 \times 10^{-8}$
26	284.2 ±0.1	275.9 ±0.1	−482 ± 19	1016 ± 195	$6.0 \times 10^{-4} \pm 8 \times 10^{-5}$	$2.5 \times 10^{-7} \pm 1 \times 10^{-8}$
27	281.3 ± 0.1	272.2 ± 0.1	−485 ± 13	990 ± 191	$5.9 \times 10^{-4} \pm 8 \times 10^{-5}$	$2.8 \times 10^{-7} \pm 1 \times 10^{-8}$
28	276.8 ± 0.1	267.1 ± 0.1	−490 ± 30	1070 ± 191	$6.2 \times 10^{-4} \pm 8 \times 10^{-5}$	$3.0 \times 10^{-7} \pm 2 \times 10^{-8}$
29	274.5 ± 0.1	263.6 ± 0.1	−499 ± 19	1189 ± 186	$6.6 \times 10^{-4} \pm 7 \times 10^{-5}$	$3.5 \times 10^{-7} \pm 2 \times 10^{-8}$
30	272.7 ± 0.1	261.0 ± 0.1	−497 ± 19	1207 ± 184	$6.7 \times 10^{-4} \pm 7 \times 10^{-5}$	$3.8 \times 10^{-7} \pm 2 \times 10^{-8}$
31	288.2 ± 0.1	279.8 ± 0.1	−557 ± 36	1261 ± 212	$7.3 \times 10^{-4} \pm 9 \times 10^{-5}$	$2.1 \times 10^{-7} \pm 2 \times 10^{-8}$
32	286.9 ±0.1	277.8 ±0.1	−558 ± 43	1176 ± 203	$6.9 \times 10^{-4} \pm 8 \times 10^{-5}$	$2.3 \times 10^{-7} \pm 2 \times 10^{-8}$
33	285.5 ±0.1	275.9 ±0.1	−566 ± 31	1121 ± 198	$6.7 \times 10^{-4} \pm 8 \times 10^{-5}$	$2.4 \times 10^{-7} \pm 2 \times 10^{-8}$
34	283.2 ±0.1	272.3 ±0.1	−572 ± 21	1054 ± 188	$6.4 \times 10^{-4} \pm 7 \times 10^{-5}$	$2.8 \times 10^{-7} \pm 1 \times 10^{-8}$
35	278.9 ±0.1	267.1 ± 0.1	−566 ± 28	1121 ± 196	$6.6 \times 10^{-4} \pm 8 \times 10^{-5}$	$3.1 \times 10^{-7} \pm 2 \times 10^{-8}$
36	276.3 ± 0.1	263.5 ± 0.1	−574 ± 59	1205 ± 186	$7.0 \times 10^{-4} \pm 8 \times 10^{-5}$	$3.5 \times 10^{-7} \pm 4 \times 10^{-8}$
37	274.8 ±0.1	260.1 ±0.1	−581± 38	1230 ± 179	$7.1 \times 10^{-4} \pm 7 \times 10^{-5}$	$4.0 \times 10^{-7} \pm 3 \times 10^{-8}$
38	291.3 ±0.1	281.1 ±0.1	−603± 23	1284 ± 163	$7.5 \times 10^{-4} \pm 7 \times 10^{-5}$	$2.3 \times 10^{-7} \pm 1 \times 10^{-8}$
39	289.4 ±0.1	279.5 ±0.1	−647± 22	1398 ± 195	$8.2 \times 10^{-4} \pm 8 \times 10^{-5}$	$2.1 \times 10^{-7} \pm 1 \times 10^{-8}$
40	288.3 ±0.1	277.7 ±0.1	−637 ± 28	1269 ± 153	$7.6 \times 10^{-4} \pm 6 \times 10^{-5}$	$2.3 \times 10^{-7} \pm 1 \times 10^{-8}$
41	287.1 ±0.1	275.9 ±0.1	−651± 120	1302 ± 154	$7.8 \times 10^{-4} \pm 8 \times 10^{-5}$	$2.4 \times 10^{-7} \pm 5 \times 10^{-8}$
42	284.1 ±0.1	272.3 ±0.1	−659± 28	1202 ± 149	$7.4 \times 10^{-4} \pm 6 \times 10^{-5}$	$2.6 \times 10^{-7} \pm 1 \times 10^{-8}$
43	281.2 ±0.1	267.6 ±0.1	−648± 24	1233 ± 154	$7.4 \times 10^{-4} \pm 6 \times 10^{-5}$	$3.1 \times 10^{-7} \pm 1 \times 10^{-8}$
44	278.2 ±0.1	263.2 ±0.1	−648± 24	1145 ± 151	$7.0 \times 10^{-4} \pm 6 \times 10^{-5}$	$3.5 \times 10^{-7} \pm 2 \times 10^{-8}$
45	275.0 ±0.1	259.6 ±0.1	−623± 70	1203 ± 155	$7.1 \times 10^{-4} \pm 7 \times 10^{-5}$	$3.9 \times 10^{-7} \pm 5 \times 10^{-8}$

TABLE V. Results from the NEMD simulations with TIP4P/2005.

T_{cold} (K)	T_{hot} (K)	T^l (K)	T^s (K)	T^g (K)	J_q' (W/m^2)	$R_{qq,0}$ (m^2 s/J K)
480	630	482.1 ±0.1	482	508 ± 5	$8.5 \times 10^7 \pm 1.0 \times 10^7$	$1.2 \times 10^{-12} \pm 2 \times 10^{-13}$
490	640	491.6 ±0.1	492	523 ± 3	$1.7 \times 10^8 \pm 8.7 \times 10^6$	$7.1 \times 10^{-13} \pm 6 \times 10^{-14}$
500	650	501.9 ± 0.2	502	542 ± 5	$2.8 \times 10^8 \pm 3.3 \times 10^7$	$5.3 \times 10^{-13} \pm 8 \times 10^{-14}$
510	660	511.7 ± 0.2	512	543 ± 3	$3.8 \times 10^8 \pm 5.6 \times 10^7$	$3.0 \times 10^{-13} \pm 5 \times 10^{-14}$
520	670	521.6 ±0.1	523	555 ± 2	$3.9 \times 10^8 \pm 1.0 \times 10^8$	$3.0 \times 10^{-13} \pm 8 \times 10^{-14}$
530	680	532.6 ± 0.2	533	552 ± 3	$5.3 \times 10^8 \pm 2.5 \times 10^7$	$1.2 \times 10^{-13} \pm 1 \times 10^{-14}$
540	690	542.3 ± 0.2	544	555 ± 2	$6.7 \times 10^8 \pm 1.5 \times 10^7$	$6.1 \times 10^{-14} \pm 8 \times 10^{-15}$
550	700	553.0 ± 0.2	556	561 ± 2	$8.4 \times 10^8 \pm 7.6 \times 10^7$	$3.2 \times 10^{-14} \pm 7 \times 10^{-15}$

[1] M. Kulmala, H. Vehkamäki, T. Petäjä, M. Dal Maso, A. Lauri, V. M. Kerminen, W. Birmili, and P. H. McMurry, J. Aerosol Sci. **35**, 143 (2004).

[2] J. Merikanto, H. Vehkamäki, and E. Zapadinsky, J. Chem. Phys. **121**, 914 (2004).

[3] F. Caupin and E. Herbert, C. R. Phys. **7**, 1000 (2006).

[4] K. Davitt, A. Arvengas, and F. Caupin, EPL **90**, 16002 (2010).

[5] F. Caupin, A. Arvengas, K. Davitt, M. El Mekki Azouzi, K. I. Shmulovich, C. Ramboz, D. A. Sessoms, and A. D. Stroock, J. Phys.: Condens. Matter **24**, 284110 (2012).

[6] Q. Zheng, D. J. Durben, G. H. Wolf, and C. A. Angell, Science **254**, 829 (1991).

[7] M. El Mekki Azouzi, C. Ramboz, J. F. Lenain, and F. Caupin, Nat. Phys. **9**, 38 (2013).

[8] G. Franzese, G. Malescio, A. Skibinsky, S. V. Buldyrev, and H. E. Stanley, Nature (London) **409**, 692 (2001).

[9] G. Franzese, M. I. Marqués, and H. E. Stanley, Phys. Rev. E **67**, 011103 (2003).

[10] B. Stevens and S. Bony, Science **340**, 1053 (2013).

[11] K. A. Emanuel, Nature (London) **401**, 665 (1999).

[12] R. B. Bird, W. E. Stewart, and E. N. Lightfoot, *Transport Phenomena* (John Wiley & Sons, New York, 2007).

[13] G. Skaugen, K. Kolsaker, H. Taxt Walnum, and Ø. Wilhelmsen, Comput. Chem. Eng. **49**, 95 (2013).

[14] S. Kjelstrup and D. Bedeaux, *Non-Equilibrium Thermodynamics of Heterogeneous Systems* (World Scientific, Singapore, 2008).

[15] C. A. Ward and G. Fang, Phys. Rev. E **59**, 429 (1999).

[16] G. Fang and C. A. Ward, Phys. Rev. E **59**, 441 (1999).

[17] C. A. Ward and D. Stanga, Phys. Rev. E **64**, 051509 (2001).

[18] C. T. Mills and L. F. Phillips, Chem. Phys. Lett. **366**, 279 (2002).

[19] C. J. Pursell and L. F. Phillips, Phys. Chem. Chem. Phys. **8**, 4694 (2006).

[20] F. Duan, V. K. Badam, F. Durst, and C. A. Ward, Phys. Rev. E **72**, 056303 (2005).

[21] V. K. Badam, V. Kumar, F. Durst, and K. Danov, Exp. Therm. Fluid Sci. **32**, 276 (2007).

[22] F. Duan, C. A. Ward, V. K. Badam, and F. Durst, Phys. Rev. E **78**, 041130 (2008).

[23] L. van der Ham, R. Bock, and S. Kjelstrup, Chem. Eng. Sci. **65**, 2236 (2010).

[24] Ø. Wilhelmsen, D. Bedeaux, S. Kjelstrup, and D. Reguera, J. Chem. Phys. **140**, 024704 (2014).

[25] Ø. Wilhelmsen, T. T. Trinh, S. Kjelstrup, T. S. van Erp, and D. Bedeaux, Phys. Rev. Lett. **114**, 065901 (2015).

[26] Ø. Wilhelmsen, D. Bedeaux, and S. Kjelstrup, Phys. Chem. Chem. Phys. **16**, 10573 (2014).

[27] J. O. Hirschfelder, C. F. Curtiss, and R. B. Bird, *Molecular Theory of Gases and Liquids* (Wiley, New York, 1966).

[28] M. Bond and H. Struchtrup, Phys. Rev. E **70**, 061605 (2004).

[29] T. Tsuruta and G. Nagayama, Therm. Sci. Eng. **10**, 9 (2002).

[30] D. Bedeaux and S. Kjelstrup, Physica A **270**, 413 (1999).

[31] H. C. Öttinger, *Beyond Equilibrium Thermodynamics* (Wiley-Interscience, New York, 2005).

[32] G. J. Snyder and E. S. Toberer, Nat. Mater. **7**, 105 (2008).

[33] F. Bresme, A. Lervik, D. Bedeaux, and S. Kjelstrup, Phys. Rev. Lett. **101**, 020602 (2008).

[34] Ø. Wilhelmsen, T. T. Trinh, S. Kjelstrup, and D. Bedeaux, J. Phys. Chem. C **119**, 8160 (2015).

[35] W. Wagner and A. Pruß, J. Phys. Chem. Ref. Data **31**, 387 (2002).

[36] P. G. Debenedetti and H. E. Stanley, Phys. Today **56**(6), 40 (2003).

[37] C. Vega, J. L. F. Abascal, and I. Nezbeda, J. Chem. Phys. **125**, 034503 (2006).

[38] J. Xu, S. Kjelstrup, D. Bedeaux, A. Røsjorde, and L. Rekvig, J. Colloid Interface Sci. **299**, 452 (2006).

[39] E. Johannessen and D. Bedeaux, Physica A **330**, 354 (2003).

[40] I. Inzoli, S. Kjelstrup, D. Bedeaux, and J. M. Simon, Chem. Eng. Sci. **66**, 4533 (2011).

[41] T. Savin, K. S. Glavatskiy, S. Kjelstrup, H. C. Öttinger, and D. Bedeaux, EPL **97**, 40002 (2012).

[42] Revised Release on the IAPS Formulation 1985 for the Thermal Conductivity of Ordinary Water Substance.

[43] F. Römer, A. Lervik, and F. Bresme, J. Chem. Phys. **137**, 074503 (2012).

[44] S. Plimpton, P. Crozier, and A. Thompson, LAMMPS: Large-Scale Atomic/Molecular Massively Parallel Simulator, Sandia National Laboratories, 2007.

[45] R. W. Hockney and J. W. Eastwood, *Computer Simulation Using Particles* (Taylor & Francis Group, New York, 1988).

[46] J. P. Ryckaert, G. Ciccotti, and H. J. C. Berendsen, J. Comput. Phys. **23**, 327 (1977).

[47] H. C. Andersen, J. Comput. Phys. **52**, 24 (1983).

[48] M. Orsi, Mol. Phys. **112**, 1566 (2014).

[49] J. M. Simon, D. Bedeaux, S. Kjelstrup, J. Xu, and E. Johannessen, J. Phys. Chem. B **110**, 18528 (2006).

[50] A. Lervik, Ø. Wilhelmsen, T. T. Trinh, and H. R. Nagel, J. Chem. Phys. **143**, 114106 (2015).

[51] D. Frenkel and B. Smit, *Understanding Molecular Simulation, From Algorithms to Applications* (Academic Press, San Diego, 2002).

[52] F. Bresme and J. Armstrong, J. Chem. Phys. **140**, 016102 (2014).

[53] K. S. Glavatskiy, Multicomponent interfacial transport as described by the square gradient model: Evaporation and condensation, Ph.D. thesis, Norwegian University of Science and Technology, 2009 .

[54] E. Magnanelli, Ø. Wilhelmsen, D. Bedeaux, and S. Kjelstrup, Phys. Rev. E **90**, 032402 (2014).

[55] G. M. Kontogeorgis, E. C. Voutsas, I. V. Yakoumis, and D. P. Tassios, Ind. Eng. Chem. Res. **35**, 4310 (1996).

[56] M. L. Michelsen and E. M. Hendriks, Fluid Phase Equilibr. **180**, 165 (2001).

[57] A. J. Queimada, C. Miqueu, I. M. Marrucho, G. M. Kontogeorgis, and J. A. P. Coutinho, Fluid Phase Equilibr. **228-229**, 479 (2005).

[58] K. S. Glavatskiy and D. Bedeaux, J. Chem. Phys. **133**, 234501 (2010).

[59] J. S. Rowlinson and B. Widom, *Molecular Theory of Capillarity* (Clarendon Press, Oxford, 1984).

[60] E. M. Blokhuis and D. Bedeaux, Mol. Phys. **80**, 705 (1993).

[61] E. M. Blokhuis and A. E. van Giessen, J. Phys.: Condens. Matter **25**, 225003 (2013).

[62] C. Vega and J. L. F. Abascal, Phys. Chem. Chem. Phys. **13**, 19663 (2011).

[63] J. Alejandre and G. A. Chapela, J. Chem. Phys. **132**, 014701 (2010).

[64] Ø. Wilhelmsen, D. Bedeaux, and D. Reguera, J. Chem. Phys. **142**, 064706 (2015).
[65] See Supplemental Material at http://link.aps.org/supplemental/10.1103/PhysRevE.93.032801 for tabulation of the interface transfer coefficients and their curvature corrections.
[66] A. Lervik, F. Bresme, and S. Kjelstrup, Soft Matter **5**, 2407 (2009).
[67] J.-L. Barrat and F. Chiaruttini, Mol. Phys. **101**, 1605 (2003).
[68] Z. Liang, W. Evans, and P. Keblinski, Phys. Rev. E **87**, 022119 (2013).
[69] B. Peng, W. He, X. Hao, Y. Chen, and Y. Liu, Comput. Mater. Sci. **87**, 260 (2014).
[70] Ø. Wilhelmsen, D. Bedeaux, and D. Reguera, J. Chem. Phys. **142**, 171103 (2015).
[71] G. A. Meehl, W. M. Washington, J. M. Arblaster, A. Hu, H. Teng, C. Tebaldi, B. N. Sanderson, J.-F. Lamarque, A. Conley, W. G. Strand, and J. B. White, J. Climate **25**, 3661 (2012).
[72] R. B. Neale, J. H. Richter, A. J. Conley, S. Park, P. H. Lauritzen, A. Gettelman, D. L. Williamson, P. J. Rasch, S. J. Vavrus, M. A. Taylor, W. D. Collins, M. Zhang, and S.-J. Lin, *Description of the NCAR Community Atmosphere Model (CAM 4.0)*, Tech. Rep. (National Center for Atmospheric Research, Boulder, CO, 2010).
[73] H. Schlichting and K. Gersten, *Boundary-Layer Theory* (Springer, Berlin, 2000).
[74] Y. A. Cengel, *Heat and Mass Transfer: A Practical Approach* (McGraw-Hill, New York, 2006).
[75] Z. Lin and S. Granick, J. Am. Chem. Soc. **127**, 2816 (2005).
[76] J. H. Weijs and D. Lohse, Phys. Rev. Lett. **110**, 054501 (2013).
[77] J. de Ruiter, R. Lagraauw, D. van den Ende, and F. Mugele, Nat. Phys. **11**, 48 (2015).
[78] X. Chen, D. Goodnight, Z. Gao, A. H. Cavusoglu, N. Sabharwal, M. DeLay, A. Driks, and O. Sahin, Nat. Commun. **6**, 7346 (2015).
[79] J. Lee, T. Laoui, and R. Karnik, Nat. Nanotechnol. **9**, 317 (2014).
[80] J. Lengyel, A. Pysanenko, V. Poterya, P. Slavíček, M. Fárník, J. Kočišek, and J. Fedor, Phys. Rev. Lett. **112**, 113401 (2014).
[81] http://www.sigma2.no.